A tomographic analysis of reflectometry data: I. Component factorization

Françoise Briolle[1,5], **Ricardo Lima**[1], **Vladimir I Man'ko**[2] **and Rui Vilela Mendes**[3,4]

[1] Centre de Physique Théorique, CNRS Luminy, case 907, F-13288 Marseille Cedex 9, France
[2] P N Lebedev Physical Institute, Leninskii Prospect 53, Moscow 117924, Russia
[3] IPFN-EURATOM/IST Association, Instituto Superior Técnico, Av. Rovisco Pais 1, 1049-001 Lisboa, Portugal
[4] CMAF, Complexo Interdisciplinar, Universidade de Lisboa, Av. Gama Pinto, 2-1649-003 Lisboa, Portugal

E-mail: francoise.briolle@univmed.fr, manko@sci.lebedev.ru and vilela@cii.fc.ul.pt

Abstract
Many signals in nature, technology and experiment have a multi-component structure. By spectral decomposition and projection on the eigenvectors of a family of unitary operators, a robust method is developed to decompose signals into their components. Different signal traits may be emphasized by different choices of the unitary family. The method is illustrated in simulated data and on data obtained from plasma reflectometry experiments in the Tore Supra.

Keywords: signal analysis, tomogram, reflectometry

(Some figures in this article are in colour only in the electronic version)

1. Introduction

Most natural and man-made signals are nonstationary and may be thought of as having a multicomponent structure. Bat echolocation, whale sounds, radar, sonar and many others are examples of this kind of signal. The notion of nonstationarity is easy to define. However, the concept of the signal component is not so clearly defined. Because time and frequency descriptions are standard methods for signal analysis, many authors have attempted to base the characterization of signal components on the analysis of the time–frequency plane. There is a large class of time–frequency signal representations (TFR). An important set of such TFRs is Cohen's class [1], obtained by convolutions with the Wigner distribution

$$C_\Phi(t, f) = \iint W(u, v)\, \Phi\left(t - u, f - v\right) \mathrm{d}u\, \mathrm{d}v \qquad (1)$$

with $W(u, v)$ being the Wigner distribution

$$W(t, f) = \int s\left(t + \frac{\tau}{2}\right) s^*\left(t - \frac{\tau}{2}\right) \mathrm{e}^{-\mathrm{i}2\pi\tau f}\, \mathrm{d}\tau. \qquad (2)$$

Once one particular TFR of the signal is constructed, the search for components may be done by looking for amplitude concentrations in the time–frequency plane. This is the methodology that has been followed by most authors [2–11]. The notions of instantaneous frequency and instantaneous bandwidth play an important role in these studies.

An important drawback of the use of TFRs is the fact that they may have negative terms, cross terms or lack the correct marginal properties in time and frequency. Even if, by the choice of a clever kernel or a smoothing or filtering operation, the TFRs are apparently free from these problems, there is no guarantee that they are free from artifacts that might lead to unwarranted inferences about the signal properties. This is a consequence of the basic fact that for time (t) and frequency $\left(\omega = \mathrm{i}\frac{\mathrm{d}}{\mathrm{d}t}\right)$, being associated with a pair of noncommuting operators, there can never be a joint probability distribution in the time–frequency plane.

Our approach to *component separation* starts from the insight that the notion of the *component* depends as much on the observer as on the observed object. That is, when we speak about a component of a signal we in fact refer to a particular feature of the signal that we want to emphasize. For

1

example, if time and frequency are the features that interest us, they might indeed be the salient features in the time–frequency plane to be identified as components. However, if it is frequency and fractality (scale) that interest us, the notion of the component and the nature of the decomposition would be completely different.

In general, the features that interest us correspond to incompatible notions (that is, to noncommuting operators). Therefore to look for robust characterizations in a joint feature plane is a hopeless task because the noncommutativity of the operators precludes the existence of joint probability densities. Instead, in our approach, we consider spectral decompositions using the eigenvectors of linear combinations of the operators. The sum of the squares of the signal projections on these eigenvectors has the same norm as the signal, thus providing an exact probabilistic interpretation. Important operator linear combinations are the time–frequency

$$B^{(S)}(\mu, \nu) = \mu t + \nu \omega = \mu t + \nu \mathrm{i} \frac{\mathrm{d}}{\mathrm{d}t}, \qquad (3)$$

the frequency-scale

$$B_1^{(A)}(\mu, \nu) = \mu \omega + \nu D = \mu \omega + \nu \frac{1}{2}(t\omega + \omega t) \qquad (4)$$

and the time-scale

$$B_2^{(A)}(\mu, \nu) = \mu t + \nu D. \qquad (5)$$

Then, a quadratic positive signal transform is defined by

$$M_s^B(X, \mu, \nu) = \int s^*(t)\delta(B(\mu, \nu) - X)s(t)\,\mathrm{d}t \qquad (6)$$

called a *B*-tomogram which, for a normalized signal

$$\int |s(t)|^2\,\mathrm{d}t = 1, \qquad (7)$$

is also normalized to

$$\int M_s^B(X, \mu, \nu)\,\mathrm{d}X = 1. \qquad (8)$$

For each (μ, ν) pair, the tomograms $M_s^B(X, \mu, \nu)$ provide a probability distribution on the variable X, corresponding to a linear combination of the chosen operators (time and frequency, frequency and scale or time and scale). Therefore, by exploring the family of operators for all pairs (μ, ν) one obtains a robust (probability) description of the signal at all intermediate operator combinations.

Using the (symmetric) operators $B(\mu, \nu)$ and their corresponding unitary exponentiations

$$U(\mu, \nu) = \exp(\mathrm{i}B(\mu, \nu)), \qquad (9)$$

a unified description of all currently known integral transforms has been obtained [12]. Explicit expressions for the tomograms in the three cases (3)–(5) may be found in [13].

Of particular interest for the component analysis in this paper is the time–frequency operator $B^{(S)}(\mu, \nu)$ for which

$$M_s(x, \mu, \nu) = \frac{1}{2\pi|\nu|} \left| \int s(t) \exp\left(\frac{\mathrm{i}\mu}{2\nu}t^2 - \frac{\mathrm{i}x}{\nu}t\right)\mathrm{d}t \right|^2 \qquad (10)$$

is called the *symplectic tomogram*. The tomogram is the homogeneous function

$$M_s\left(\frac{x}{p}, \frac{\mu}{p}, \frac{\nu}{p}\right) = |p|M_s(x, \mu, \nu). \qquad (11)$$

For the particular case of $\mu = \cos\theta, \nu = \sin\theta$, the symplectic tomogram coincides with the Radon transform [14], which has already been used for signal analysis by several authors [15–17] in a different context.

Once a tomogram for a linear combination of operators O_1 and O_2 ($B = \mu O_1 + \nu O_2$) is constructed, what one obtains in the $(X, (\mu, \nu))$ (hyper-) plane is an image of the probability flow from the O_1-description of the signal to the O_2-description, through all the intermediate steps of the linear combination. In contrast with the time–frequency representations we need not worry about cross terms or artifacts, because of the exact probability interpretation of the tomogram. Then, we may define as a *component of the signal* any distinct feature (ridge, peak, etc) of the probability distribution in the $(X, (\mu, \nu))$ (hyper-) plane. It is clear that the notion of the component is contingent on the choice of the pair (O_1, O_2).

In section 2 we analyze in detail the time–frequency tomogram, the choice of a complete orthogonal basis of eigenvectors of $B^S(\mu, \nu)$ for the projection of the signal and how the component identification may be carried out by spectral decomposition into subsets of this basis. In section 3 a few examples of component decomposition of noisy signals are worked out, which show the effectiveness of the method.

Depending on the choice of operators that enter into B, the method seems to be of general utility for feature identification and component separation. We must also point out that, if more than two features are relevant, we might use in B linear combinations of more operators. Also, these operators need not be obtained from differential operators in time only. Using operators that involve both time and space, and a similar construction, space–time features may be identified.

Here, in section 4, we make a concrete application to experimental data obtained in the reflectometry analysis of plasma density. From the way these data are collected, by sending a variable frequency signal to the plasma for a short interval and detecting its reflection, it is likely that the time–frequency tomogram, associated with $B^{(S)}(\mu, \nu)$, will be the most appropriate. The results of out analysis seem to confirm this hypothesis. For other signals, for example those with a multiscale nature, it is probably the tomogram associated with $B_2^{(A)}(\mu, \nu)$ that might provide the better insight.

In the appendices we collect a few results, which are useful for the practical calculation of the symplectic tomograms.

2. Tomograms and signal analysis

Here we describe in detail the method of component separation for the case of $B^{(S)}(\mu, \nu)$. Following the ideas described in the introduction, a probability family of distributions, $M_s(x, \theta)$,

is defined from a (general) complex signal $s(t)$, $t \in [0, T]$ by

$$M_s(x, \theta) = \left| \int s(t) \Psi_x^{\theta,T}(t) \, dt \right|^2 = \left| \langle s, \Psi_x^{\theta,T} \rangle \right|^2 \qquad (12)$$

with

$$\Psi_x^{\theta,T}(t) = \frac{1}{\sqrt{T}} \exp \left(\frac{-i \cos \theta}{2 \sin \theta} t^2 + \frac{ix}{\sin \theta} t \right). \qquad (13)$$

This is a particular case of equation (10) for $\mu = \cos \theta$, $\nu = \sin \theta$. Here θ is a parameter that interpolates between the time and the frequency operators, thus running from 0 to $\pi/2$ whereas x is allowed to be any real number. Note that the $\Psi_x^{\theta,T}$ are generalized eigenfunctions of $B^{(S)}(\theta) = t \cos \theta + i \sin \theta \frac{d}{dt}$ for any spectral value x. Therefore $M_s(x, \theta)$ is a (positive) probability distribution as a function of x for each θ. From an abstract point of view, since for different θ's the $U(\theta)$ (see equation (9)) are unitarily equivalent operators, all the tomograms share the same information. However, from a practical point of view the situation is somehow different. In fact when θ changes from 0 to $\pi/2$ the information on the time localization of the signal will gradually concentrate on large x values which are unattainable because of sampling limitations. On the other hand and by opposite reasons, close to $\theta = 0$ the frequency information is lost. Therefore we search for intermediate values of θ where a good compromise may be found. For such intermediate values, as we shall see in several examples, it is possible to pull apart different components of the signal that take into account both time and frequency information. The reason why this is the case will be clear by looking at the properties of (13).

First we select a subset x_n in such a way that the corresponding family $\{ \Psi_{x_n}^{\theta,T}(t) \}$ is orthogonal and normalized,

$$\langle \Psi_{x_m}^{\theta,T}, \Psi_{x_n}^{\theta,T} \rangle = \delta_{m,n}. \qquad (14)$$

This is possible by taking the sequence

$$x_n = x_0 + \frac{2n\pi}{T} \sin \theta, \qquad (15)$$

where x_0 is freely chosen (in general we take $x_0 = 0$ but it is possible to make other choices, depending on what is more suitable for the signal under study).

A glance at the shape of the functions (13) shows that the nodes (the zero crossings) t_n of the real (resp. imaginary) part of $\Psi_{x_n}^{\theta,T}$ are the solutions of

$$\frac{\cos \theta}{2 \sin \theta} t_n^2 - \frac{x}{\sin \theta} t_n = 2\pi n \qquad (\text{resp. } 2\pi n + \pi/2). \quad (16)$$

It is clear that $|t_{n+1} - t_n|$ scales as $\sqrt{n}$ and that, for fixed θ, the oscillation length at a given t decreases when $|x|$ increases. As a result, the projection of the signal on the $\{ \Psi_{x_n}^{\theta,T}(t) \}$ will locally explore different scales. On the other hand, changing θ will modify the first term of (16) in such a way that the local time scale is larger when θ becomes larger in agreement with the uncertainty principle.

We then consider the projections of the signal $s(t)$

$$c_{x_n}^{\theta}(s) = \langle s, \Psi_{x_n}^{\theta,T} \rangle \qquad (17)$$

which in the following are used for signal processing purposes. In particular a natural choice for denoising consists in eliminating the $c_{x_n}^{\theta}(s)$ such that

$$\left| c_{x_n}^{\theta}(s) \right|^2 \leqslant \epsilon \qquad (18)$$

for some chosen threshold ϵ, the remainder being used to reconstruct a denoised signal. In this case a proper choice of θ is an important issue in the method.

In the present work we mainly explore the spectral decomposition of the signal to perform a multi-component analysis. This is done by selecting subsets $\mathcal{F}_k$ of the x_n and reconstructing partial signals (k-components) by restricting the sum to

$$s_k(t) = \sum_{n \in \mathcal{F}_k} c_{x_n}^{\theta}(s) \Psi_{x_n}^{\theta,T}(t) \qquad (19)$$

for each k.

Equation (19) builds the signal components as spectral projections of s. As we shall see, by an appropriate choice of θ, it is possible to use this technique to disentangle the different components of a signal.

Note that the inverse of $\left| t_{n+1}^{\theta} - t_n^{\theta} \right|$ plays the role of a quasi-instantaneous frequency defined in a θ-like scale. This is a piecewise constant function but, as seen from (13), it grows approximately linearly in time with slope $\tan^{-1}(\theta)$. We used such time scales to control the quality of the sampling.

3. Examples: simulated data

In this section we discuss the general method presented in the previous section in two particular simulated signals. The first example shows how the method is able to disentangle a signal with different time and frequency components. In the second example a signal with time-varying frequency is analyzed.

3.1. First example

Let us consider a signal $y(t)$, of duration $T = 20$ s, that is the sum of three sinusoidal complex signals y_k, $k = 1, 2, 3$, plus a noise component b:

$$y(t) = y_1(t) + y_2(t) + y_3(t) + b(t), \qquad (20)$$

where

$$y_1(t) = \exp(i25t), \quad t \in [0, 20]$$
$$y_2(t) = \exp(i75t), \quad t \in [0, 5]$$
$$y_3(t) = \exp(i75t), \quad t \in [10, 20].$$

The signal-to-noise ratio, $\text{SNR}_{y,b}$, is about 10 dB, the SNR being defined by

$$\text{SNR}(y, b) = 10 \log_{10} \frac{P_y}{P_b} \qquad (21)$$

with $P_y = \frac{1}{T} \int_0^T |y(t)|^2 \, dt$ and $P_b = \frac{1}{T} \int_0^T |b(t)|^2 \, dt$. The real part of the simulated data, $\mathcal{R}[y(t)]$, is shown in figure 1. In order to test the robustness of the projection protocol we first compare the original signal $y(t)$ with a reconstructed signal $\tilde{y}(t)$ given by

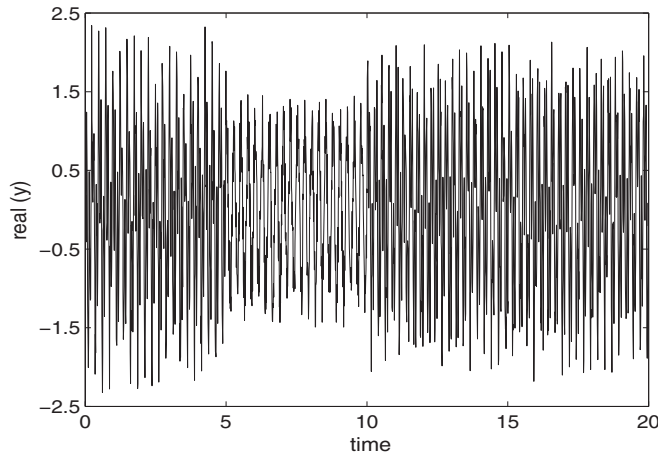$$\tilde{y}(t) = \sum_{x_n = -175}^{175} c_{x_n}^{\theta}(y) \Psi_{x_n}^{\theta,T}(t). \qquad (22)$$

Figure 1. Temporal representation of the real part $\mathcal{R}\,[y(t)]$ of the simulated data from equation (20).

Figure 2. $c_{x_n}^{\theta}(y)$ spectrum of the simulated data $y(t)$ for $\theta = \frac{\pi}{5}$ and $-30 \leqslant x_n \leqslant 100$.

The quadratic error $E(y, \tilde{y})$, between the original and the reconstructed signal is less than -27 dB. The quadratic error is defined as

$$E(y, \tilde{y}) = 10 \log_{10} \frac{P_{y-\tilde{y}}}{P_y}. \tag{23}$$

The quadratic error grows to -22 dB if the reconstruction is limited to the range used for the component analysis below (i.e., $45 \leqslant x_n \leqslant 155$).

The value $\theta = \frac{\pi}{5}$ is chosen by direct inspection of the tomogram of the signal $y(t)$. In this case one sees three well-separated spectral components (figure 2). Clearly this is not the unique possible choice. We may try different choices of θ knowing that the incertitude on the time support will increase with θ whereas the quasi-local frequency incertitude will decrease. From a practical point of view, the only sound rule is that, if component separation is the goal, then one should choose a θ for which separated concentrations of probability are apparent. Given the existence of a unitary transformation between the $\left\{\Psi_{x_n}^{\theta,T}(t)\right\}$ basis for different θ, the reconstruction of the components will be essentially the same as long as we remain in the θ-interval for which well-separated concentrations of the probability are manifest.

In this example, we performed the factorization of $y(t)$ into three components $\tilde{y}_1(t)$, $\tilde{y}_2(t)$ and $\tilde{y}_3(t)$ defined respectively by equations (24), (25) and (26). Using different values of θ, the quadratic errors $E(y, \tilde{y})$, $E(y_1, \tilde{y}_1)$, $E(y_2, \tilde{y}_2)$ and $E(y_3, \tilde{y}_3)$ are computed (equation (23)). We summarize the corresponding data in table 1.
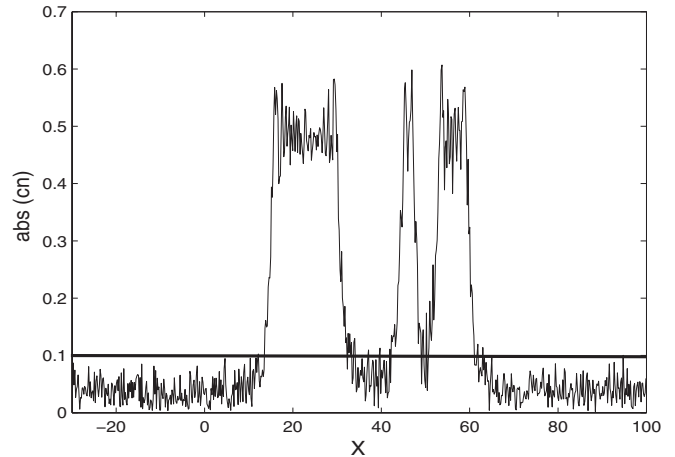
In this example, by looking at the data presented in table 1, the choice of $\theta = \frac{\pi}{5}$ to carry out the factorization provides a good performance. Then we simply apply an energy threshold $\epsilon = 0.1$, which is about 15% of the energy level of the signal, to decompose the signal y into three components (figure 2).

The first component, $\tilde{y}_1(t)$, corresponds to the spectral range $10 \leqslant x_n \leqslant 35$:

$$\tilde{y}_1(t) = \sum_{x_n=10}^{35} c_{x_n}^{\theta}(y)\Psi_{x_n}^{\theta,T}(t). \tag{24}$$

The second component, $\tilde{y}_2(t)$, corresponds to the spectral range $40 \leqslant x_n \leqslant 50$:

$$\tilde{y}_2(t) = \sum_{x_n=40}^{50} c_{x_n}^{\theta_0}(y)\Psi_{x_n}^{\theta_0,T}(t). \tag{25}$$

The real parts of $y_2(t)$ and $\tilde{y}_2(t)$ are presented in figure 3.

The last component, $\tilde{y}_3(t)$, corresponds to the spectral range $40 \leqslant x_n \leqslant 65$:

$$\tilde{y}_3(t) = \sum_{x_n=40}^{65} c_{x_n}^{\theta}(y)\Psi_{x_n}^{\theta,T}(t). \tag{26}$$

Figure 4 gives a representation of both $\mathcal{R}\,[y_3(t)]$ and $\mathcal{R}\,[\tilde{y}_3(t)]$.

The quadratic errors $E(y_1, \tilde{y}_1)$, $E(y_2, \tilde{y}_2)$ and $E(y_3, \tilde{y}_3)$ can be read from table 1. They are, respectively, -17.5 dB, -12.5 dB and -14 dB.

For comparison, the projection of the simulated data $y(t)$ in the frequency domain $\left(\theta_0 = \frac{\pi}{2}\right)$, presented in figure 5, shows

Table 1. Quadratic errors computed from equation (23).

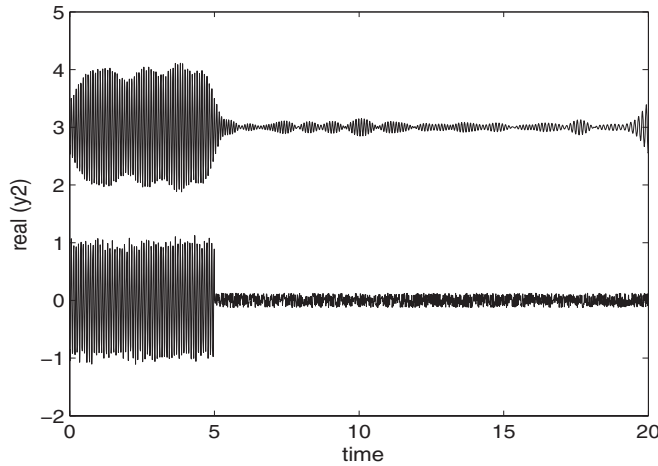| θ	$\pi/8$	$\pi/5$	$3\pi/10$	$4\pi/5$	$\pi/2$
$E(y_1, \tilde{y}_1)$	-14.5 dB	-17.5 dB	-18.5 dB	-17.5 dB	-12.5 dB
$E(y_2, \tilde{y}_2)$	-10.5 dB	-12.5 dB	-9 dB	-7 dB	-0.5 dB
$E(y_3, \tilde{y}_3)$	-14.5 dB	-14 dB	-13.5 dB	-7 dB	-4 dB
$E(y, \tilde{y})$	-26.5 dB	-27 dB	-30 dB	-30 dB	-28 dB

Figure 3. $\mathcal{R}[y_2(t)]$ and $\mathcal{R}[\tilde{y}_2(t)]$. For visual purposes, the mean value of $\mathcal{R}[\tilde{y}_2(t)]$ is shifted to 3.
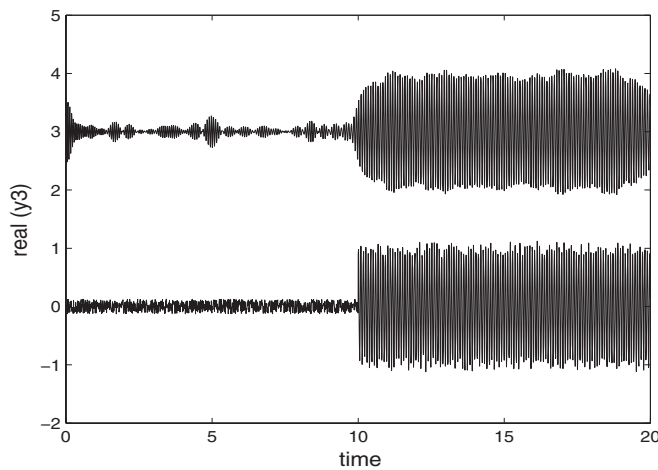

Figure 4. Representation of $\mathcal{R}[y_3(t)]$ and $\mathcal{R}[\tilde{y}_3(t)]$. For visual purposes, the mean value of $\mathcal{R}[\tilde{y}_3(t)]$ is shifted to 3.

that the factorization in three components is not possible: only two components can be extracted from this projection. At the frequency $x_n = 25$ rad s^{-1}, the component will be equal to $\tilde{y}_1(t)$. At the frequency $x_n = 75$ rad s^{-1}, it is impossible to separate $y_2(t)$ and $y_3(t)$ and the component will be equal to $\tilde{y}_2(t) + \tilde{y}_3(t)$.

3.2. Second example

Here we analyze the decomposition into elementary components of another signal which aims to mimic, in a simplified way, the case of an incident plus a reflected wave delayed in time and with an acquired time-dependent change in phase. In this case the simulated signal $y(t)$ is the sum of an 'incident' chirp $y_0(t)$ and a 'deformed reflected' chirp $y_R(t)$. White noise is added to the signal. The incident chirp is

$$y_0(t) = e^{i\Phi_0(t)}, \qquad (27)$$

with $\Phi_0(t) = a_0 t^2 + b_0 t$.

The 'instantaneous frequency' of $y_0(t)$ sweeps linearly from 75 rad s^{-1} to 50 rad s^{-1} over 20 s. Its phase derivative is linearly dependent on time: $\frac{d}{dt}\Phi_0(t) = 2a_0 t + b_0$.
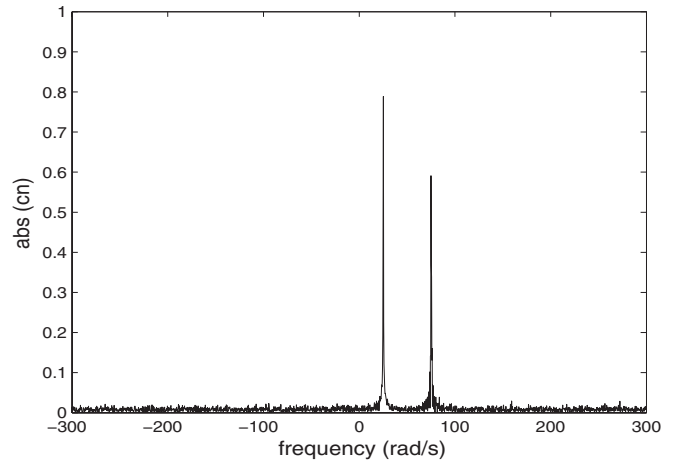

Figure 5. Projection $c_{x_n}^{\theta_0}$ of the signal for $\theta_0 = \frac{\pi}{2}$.
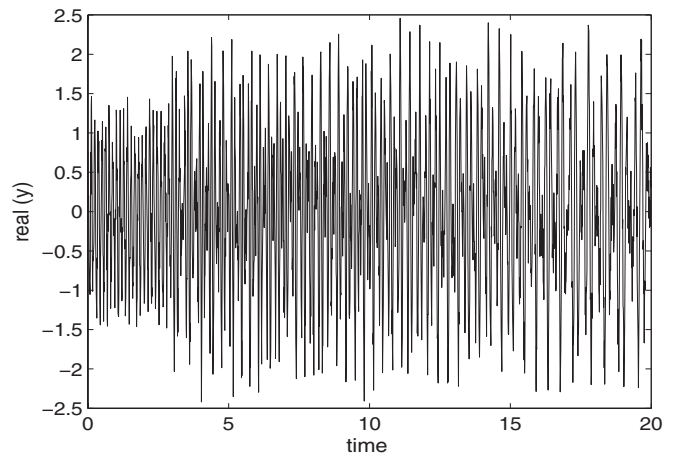

Figure 6. Temporal representation of the real part $\mathcal{R}[y(t)]$ of the simulated data defined by equation (29).

The 'reflected' signal $y_R(t)$ is delayed by $t_R = 3$ s from the incident one and continuously sweeps from 75 rad s^{-1} to 50 rad s^{-1}:

$$y_R(t) = e^{i\Phi_R(t)}, \qquad (28)$$

with $\Phi_R(t) = a_R(t - t_R)^2 + b_R(t - t_R) + 10(t - t_R)^{\frac{3}{2}}$. In this case the phase derivative $\frac{d}{dt}\Phi_R(t)$ is not a linear function. This signal is zero during the first 3 s seconds and ends at $t = 23$ s.

The simulated signal is defined by

$$y(t) = y_0(t) + y_R(t) + b(t). \qquad (29)$$

The signal-to-noise ratio, SNR(y, b), is 15 dB. The real $\mathcal{R}[y(t)]$ part of this signal is shown in figure 6.

Figure 7 shows $\frac{d}{dt}\Phi_0(t)$ and $\frac{d}{dt}\Phi_R(t)$ as a function of time. Note that, except for the first three seconds, there is an almost complete overlap of the 'instantaneous frequency' of the signals $y_0(t)$ and $y_R(t)$.

The tomogram of the first 20 s of $y(t)$, $M_y(\theta, x) = \left|\langle y, \Psi_x^{\theta, T}\rangle\right|^2$, has a maximum at $\sin(\theta) \approx 0.625$ (figure 8) corresponding to the 'incident' part of the signal that mainly projects in the unique $\Psi_x^{\theta, T}$ that matches $\Phi_0(t)$. We take the
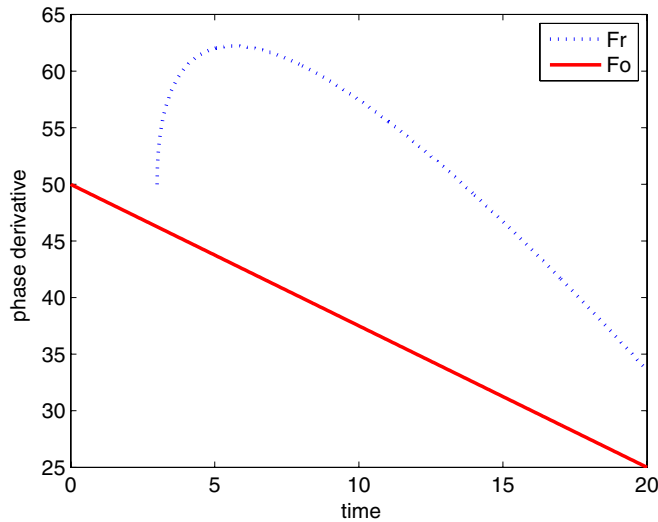
Figure 7. Representation of $F_o = \frac{d}{dt}\Phi_0(t)$ and $F_r = \frac{d}{dt}\Phi_R(t)$ as a function of time.
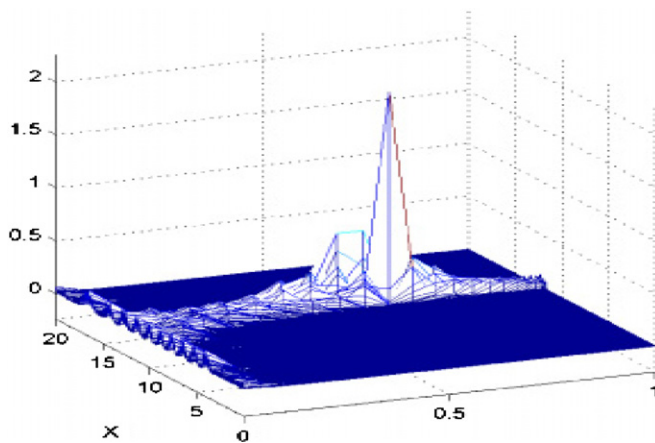

Figure 8. Tomogram of the simulated data defined by equation (29).

value of $\sin(\theta) \approx 0.625$ to carry out the separation of $y(t)$ into its components.

The corresponding spectrum $c_{x_n}^{\theta}(y)$ is shown in figure 9. Based on this spectrum we decompose the signal into two spectral components.

From the first component we reconstruct the 'incident' chirp $y_0(t)$ by

$$\tilde{y}_0(t) = \sum_{x_n=45}^{47.25} c_{x_n}^{\theta_0}(y)\Psi_{x_n}^{\theta_0,T}(t). \tag{30}$$

The quadratic error, between $\tilde{y}_0(t)$ and $y_0(t)$, $E(y_0, \tilde{y}_0)$, is -9.5 dB.

From the second spectral component we reconstruct the 'reflected' chirp given by

$$\tilde{y}_R(t) = \sum_{x_n=47.5}^{50.5} c_{x_n}^{\theta}(y)\Psi_{x_n}^{\theta,T}(t). \tag{31}$$

In this case the quadratic error $E(y_R, \tilde{y}_R)$ is -10 dB. This may be compared with a quadratic error $E(y, \tilde{y})$ of -29 dB for the total signal reconstructed from the spectral projection corresponding to $45 < x_n < 50.5$.
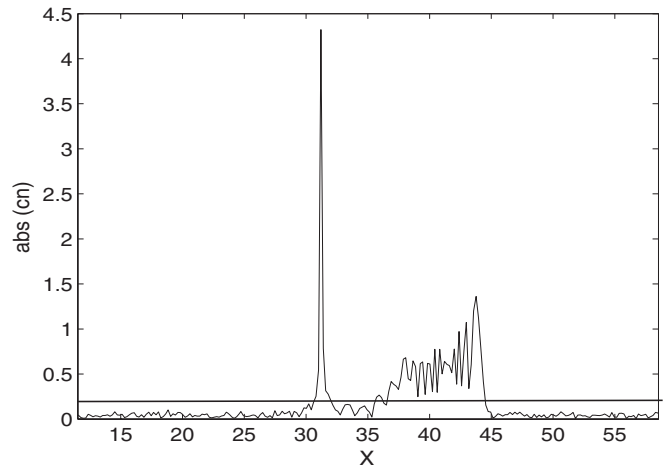

Figure 9. Spectrum of the signal for $\sin(\theta) = 0.625$.

We have tested the method with different delays that encode for the distance of the two 'frequencies'. The quality of the disentanglement deteriorates when the delay decreases. But it can still be done for a delay as short as 1 s. Therefore we conclude that the method is quite robust.

4. An application to reflectometry data. Component analysis

We now use signals coming from reflectometry measurement in plasma physics, to show the ability of the tomogram method to separate different components of the signal to which it is then possible to assign a clear physical meaning. The reflectometry diagnostic is widely used to determine the electronic density profile in a tokamak. The principle, based upon a radar technique [18], is to measure the phase of a probing wave reflected by the plasma cut-off layer at a given density, where the refractive index goes to zero. The determination of the density profile can be achieved by continuously sweeping the frequency of the probing wave.

Different techniques are used to measure the density profile on fusion plasmas [19] (phase difference, ultrashort pulses, continuous sweep, ...). A broadband reflectometer operating in the frequency range 50–75 GHz (V band) [20, 21] and 75–110 GHz (W band) [22] has been developed on Tore Supra to measure the electron density profiles at the edge.

The sweep frequency reflectometry system of Tore Supra launches a probing wave on the extraordinary mode polarization (X mode) in the V band (50–75 GHz). The emitting and receiving antennas are located at about 1.20 m from the plasma edge outside the vacuum vessel. The reflectometry system operates in the burst mode, i.e. the sweeps are performed repeatedly every 25 μs. The duration of one sweep, $E_0(t) = A_0\, e^{i\phi(t)}$, is 20 μs and 5000 chirps are sent during one measurement. During the 20 μs measurement time, the frequency of the probing wave continuously varies from 50 GHz to 75 GHz (V band).

The heterodyne reflectometers, with I/Q detection, provide a good signal-to-noise ratio, up to 40 dB. For each sweep, the reflected chirp $E_R(t)$ is mixed with the incident
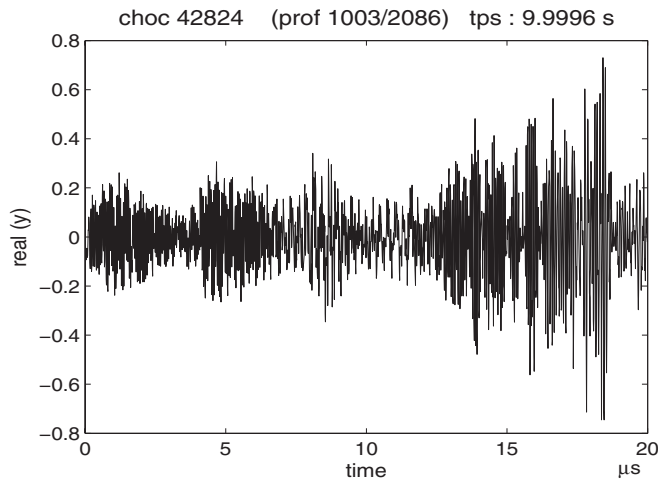
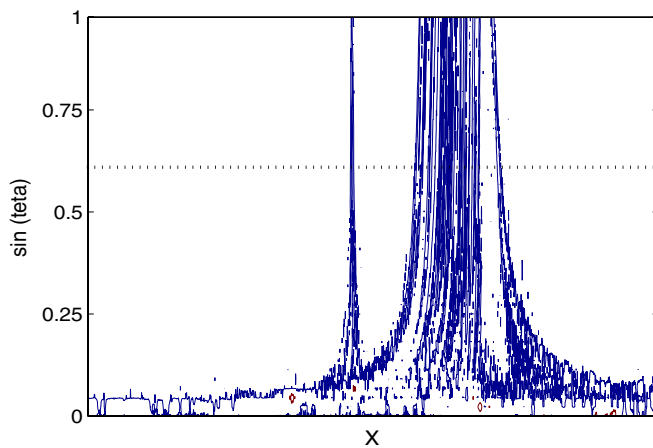**Figure 10.** Time representation of the reflectometry signal.

Figure 11. Contour plot of the tomogram of the reflectometry signal $(M_y(x, \theta) \geqslant 0.01)$.

sweep $E_0(t)$ and only the interference term is recorded as in-phase and 90° phase shifted signals sampled at $T_e = 10^{-8}$ s

$$x_1(t) = A_0 A_R(t) \cos(\varphi(t))$$
$$x_2(t) = A_0 A_R(t) \sin(\varphi(t)).$$

For each sweep, the phase $\varphi(t)$ of the reflected signal is represented by

$$y(t) = x_1(t) + \mathrm{i}x_2(t) = A(t)\, \mathrm{e}^{\mathrm{i}\varphi(t)}. \tag{32}$$

The amplitude of this signal $A(t) = A_0 A_R(t)$ is of low frequency. The real part of one such signal $y(t)$ is shown in figure 10.

The contour plot of the tomogram $M_y(x, \theta)$ of the signal is shown in figure 11 where it is possible to see that it carries three main components. The choice of $\sin(\theta) = 0.58$ to perform the factorization of the signal was done by the inspection of this tomogram. The spectrum $c_{x_n}^\theta(y)$ of the reflectometry signal for $\sin(\theta) = 0.58$ is shown in figure 12. When reconstructing $\tilde{y}(t)$ by

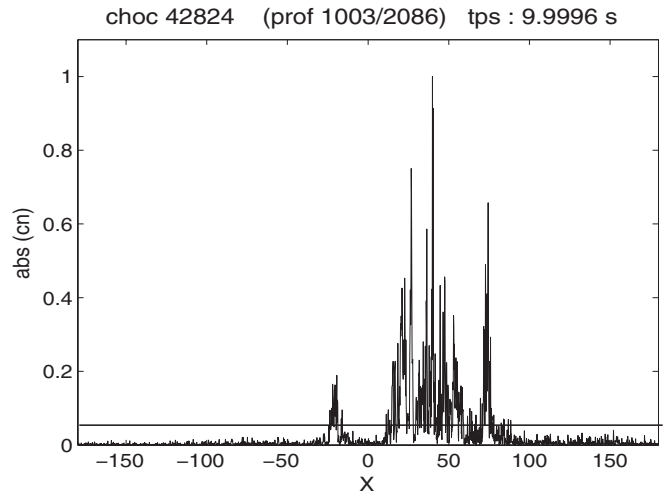$$\tilde{y}(t) = \sum_{x_n=-200}^{200} c_{x_n}^\theta(y) \Psi_{x_n}^{\theta,T}(t) \tag{33}$$

Figure 12. Spectrum $c_{x_n}^\theta$ of the reflectometry signal $y(t)$ for $\sin(\theta) = 0.58$.
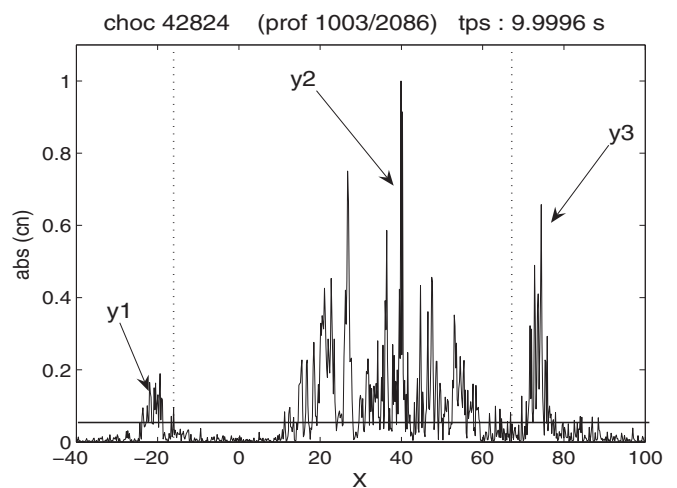

Figure 13. Part of the spectrum $c_{x_n}^\theta(y)$ of the reflectometry signal used in the factorization.

the quadratic error $E(y, \tilde{y})$ between the original and the reconstructed signals is -25 dB.

Factorization of the reflectometry signal. By taking a threshold equal to $\epsilon = 0.04$ we select the spectral components corresponding to $|c_{x_n}| \neq 0$ for $-40 \leqslant x_n \leqslant 100$ (see figure 13). The error between the original and the selected signal is about -18 dB. From there the spectrum of $y(t)$ splits into three components.

First component, the reflection on the porthole. The first component, $\tilde{y}_1(t)$ corresponds to $-20 \leqslant x_n \leqslant 0$ and is therefore defined as

$$\tilde{y}_1(t) = \sum_{x_n=-20}^{0} c_{x_n}^\theta(y) \Psi_{x_n}^\theta(t). \tag{34}$$

It is a low-frequency signal corresponding to the heterodyne product of the probe signal with the reflection on the porthole [22]. It is shown in figure 14.
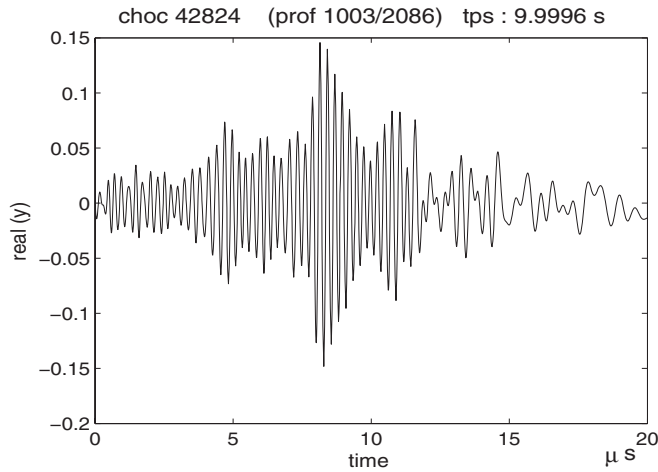
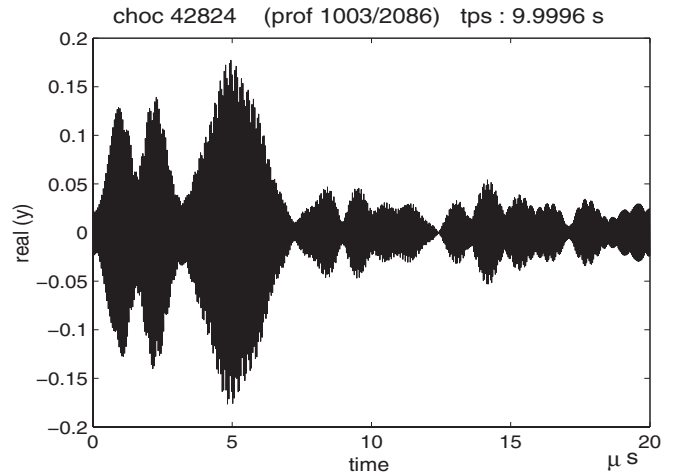**Figure 14.** First component of the reflectometry signal corresponding to the reflection on the porthole.

Figure 15. Second component of the reflectometry signal, corresponding to the reflection on the plasma.

Figure 16. Third component of the reflectometry signal, corresponding to reflection on the wall of the vacuum vessel
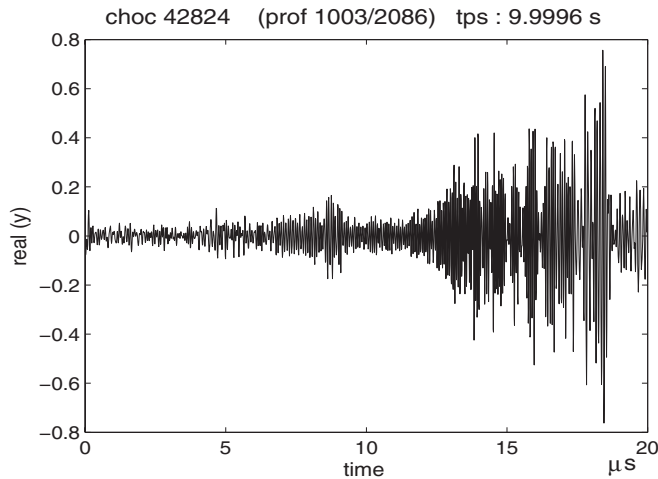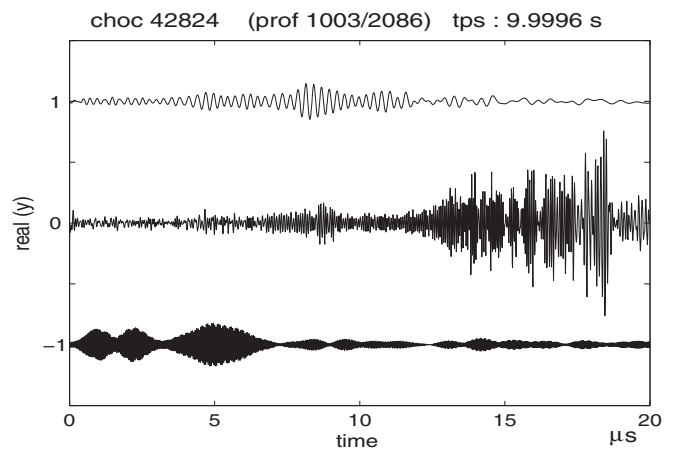

Figure 17. The three components of the reflectometry signal. For visual purposes, the average of $\tilde{y}_1(t)$ is shifted to 1 and the average of $\tilde{y}_3(t)$ to -1.

Second component, the plasma signal. The second component has a Fourier spectra that fits the expected behavior corresponding to the reflection of the wave inside the plasma of the tokamak [22]. This component, $\tilde{y}_2(t)$, corresponds to $0 \leqslant x_n \leqslant 110$ and is therefore defined as

$$\tilde{y}_2(t) = \sum_{x_n=0}^{110} c_{x_n}^{\theta}(y) \Psi_{x_n}^{\theta}(t). \tag{35}$$

It is shown in figure 15.

Third component, the first reflection on the wall of the vacuum vessel. The last component corresponds [22] to the first reflection on the wall of the vacuum vessel. This component, $\tilde{y}_3(t)$, corresponds to $110 \leqslant x_n \leqslant 140$ and is therefore defined as

$$\tilde{y}_3(t) = \sum_{x_n=10}^{140} c_{x_n}^{\theta}(y) \Psi_{x_n}^{\theta}(t). \tag{36}$$

This component is shown in figure 16.

We note that by undertaking a new factorization of this third component it seems possible to separate different successive reflections of the wave but this would be out of the scope of this work.

The three components of the reflectometry signal are presented together on the same plot (figure 17). It is instructive to compare this factorization with the original reflectometry signal (see figure 10).

5. Conclusions

Based on a complete and probabilistically rigorous spectral analysis and projection on the eigenvectors of a family of unitary operators, our method seems quite robust to disentangle the relevant components of the signals. This has been demonstrated both on simulated and on experimental reflectometry data. In particular in this last case, a clear identification of the physical origin of the components and their separation is readily achieved. Such separation could not be achieved by the simple filtering techniques. In the analysis

of reflectometry data, component separation and denoising is a required first step to obtain reliable information on the plasma density. In particular, accuracy in these measurements is quite critical if in addition to the average local density one also wants to have information on plasma fluctuations and turbulence.

After the component separation phase, the method also provides by truncation of some subsets of the projection coefficients a very flexible denoising technique.

Another important conclusion from this study is the fact that by the choice of different families of (unitary) operators and their spectral representations, different traits and components of the signals may be emphasized.

Acknowledgments

Appendix A. Gauss–Hermite decomposition of the tomograms

From the definition (10) of the tomogram transform one sees that the calculation from the data near $\nu = 0$ has accuracy problems because of the fast variation of the phase in (10). Two techniques are used to deal with this problem. The first one uses a projection of the time signal $s(t)$ on an orthogonal basis and the second uses the homogeneity properties (11) and an expansion of the Fresnel tomogram near $\nu = 0$. The first technique is described in this appendix and the second in appendix B.

Let $s(t)$ be a normalized signal

$$\int |s(t)|^2 \, \mathrm{d}t = 1. \tag{A.1}$$

Decompose the signal into Gauss–Hermite polynomials

$$s(t) = \sum_{n=0}^{\infty} c_n(t)\psi_n(t), \tag{A.2}$$

with

$$\psi_n(t) = \frac{\mathrm{e}^{-t^2/2}}{\pi^{1/4}} \frac{1}{\sqrt{2^n n!}} H_n(t) \tag{A.3}$$

and

$$c_n = \int s(t)\psi_n(t) \, \mathrm{d}t. \tag{A.4}$$

Then, the tomogram of the signal is

$$M_s(X, \mu, \nu) = M_0(X, \mu, \nu)$$
$$\times \left| \sum_{n=0}^{\infty} c_n \frac{1}{\sqrt{n!}} \left(\frac{1}{2} - \frac{1}{1 - \mathrm{i}\mu/\nu} \right)^{n/2} H_n\left(\frac{b}{2\sqrt{k}} \right) \right|^2, \tag{A.5}$$

with

$$M_0(X, \mu, \nu) = \frac{1}{\sqrt{\pi(\mu^2 + \nu^2)}} \, \mathrm{e}^{-X^2/(\mu^2+\nu^2)} \tag{A.6}$$

and

$$b = \frac{\mathrm{i}\sqrt{2}X}{\mathrm{i}\mu - \nu}, \qquad k = \left(\frac{1}{2} - \frac{1}{1 - \mathrm{i}\mu/\nu} \right). \tag{A.7}$$

Appendix B. The Fresnel tomogram

The symplectic tomogram $M_s(X, \mu, \nu)$ can be reconstructed if one knows the (Fresnel) tomogram [23]

$$M_{\mathrm{F}}(X, \nu) = M_s(X, 1, \nu) \tag{B.1}$$

due to the homogeneity property (11). In fact, one has

$$M_s(X, \mu, \nu) = \frac{1}{|\mu|} M_s\left(\frac{X}{\mu}, 1, \frac{\nu}{\mu} \right), \tag{B.2}$$

which means that, if one knows $M_{\mathrm{F}}(\tilde{X}, \tilde{\nu})$, the symplectic tomogram is obtained by replacement and a factor,

$$M_s(X, \mu, \nu) = \frac{1}{|\mu|} M_{\mathrm{F}}\left(\tilde{X} \to \frac{X}{\mu}, \tilde{\nu} \to \frac{\nu}{\mu} \right). \tag{B.3}$$

In terms of the signal $s(t)$ it reads

$$M_{\mathrm{F}}(X, \nu) = \frac{1}{2\pi|\nu|} \left| \int \mathrm{e}^{\mathrm{i}(X-y)^2/2\nu} s(y) \, \mathrm{d}y \right|^2$$
$$= \left| \int \frac{1}{\sqrt{2\pi|\nu|}} \mathrm{e}^{\mathrm{i}(X-y)^2/2\nu} s(y) \, \mathrm{d}y \right|^2$$
$$= \left| \exp\left[-\mathrm{i}\nu\left(-\frac{1}{2}\frac{\partial^2}{\partial X^2} \right) \right] s(X) \right|^2. \tag{B.4}$$

Thus for small ν one has

$$M_s(X, \mu, \nu) \approx \frac{1}{|\mu|} \left| s\left(\frac{X}{\mu} \right) - \frac{\mathrm{i}\nu}{2} s''\left(\frac{X}{\mu} \right) \right|^2. \tag{B.5}$$

In the Gauss–Hermite basis it is

$$M_{\mathrm{F}}(X, \nu) = \frac{\mathrm{e}^{-X^2/(1+\nu^2)}}{\sqrt{\pi(1+\nu^2)}}$$
$$\times \left| \sum_{n=0}^{\infty} c_n \frac{1}{\sqrt{n!}} \left(\frac{1}{2} - \frac{1}{1 - \mathrm{i}/\nu} \right)^{n/2} H_n\left(\frac{\tilde{b}}{2\sqrt{\tilde{k}}} \right) \right|^2, \tag{B.6}$$

with

$$\tilde{b} = \frac{\mathrm{i}\sqrt{2}X}{\mathrm{i} - \nu}, \qquad \tilde{k} = \left(\frac{1}{2} - \frac{1}{1 - \mathrm{i}/\nu} \right). \tag{B.7}$$

As a series, the Fresnel tomogram is

$$M_F(X, \nu) \approx \left| \sum_{k=0}^{\infty} \left(\frac{\mathrm{i}\nu}{2} \right)^k \frac{1}{k!} \frac{\mathrm{d}^{2k} f(X)}{\mathrm{d}X^{2k}} \right|^2, \tag{B.8}$$

leading to a symplectic tomogram

$$M(X, \mu, \nu) = \frac{1}{|\mu|} \left| \sum_{k=0}^{\infty} \left(\frac{\mathrm{i}\nu}{2\mu} \right)^k \frac{1}{k!} \frac{\mathrm{d}^{2k} f(X/\mu)}{\mathrm{d}X^{2k}} \right|^2. \tag{B.9}$$

Since

$$-\frac{1}{2}\frac{\partial^2}{\partial t^2} s_n(t) + \frac{t^2}{2} s_n(t) = \left(n + \frac{1}{2} \right) s_n(t),$$
$$n = 0, 1, 2, \ldots, \tag{B.10}$$

one has, for small ν, the following Fresnel tomogram of $s_n(t)$:

$$M_n(X, \mu = 1, \nu) \approx s_n^2(X) \left[1 + \left(n + \frac{1}{2} - \frac{X^2}{2} \right) \nu^2 \right]. \tag{B.11}$$

References

[1] Cohen L 1989 Time–frequency distributions: a review *Proc. IEEE* **77** 941–81

[2] Cohen L 1992 What is a multi-component signal? *IEEE Proc. Int. Conf. Acoust. Speech Signal Process. '92* **vol 5** pp 113–6

[3] Khadra L M 1989 Time–frequency distribution of multi-component signals *Int. J. Electron.* **67** 53–7

[4] Choi H I and Williams W J 1989 Improved time–frequency representation of multi-component signals using exponential kernels *IEEE Trans. Acoust. Speech Signal Process.* **37** 862–71

[5] Fineberg A B and Mammone R J 1991 Detection and classification of multicomponent signals *Proc. 25th Asilomar Conf. on Computer, Signal and Systems* pp 1093–7

[6] Jones G and Boashash B 1990 Instantaneous frequency, instantaneous bandwidth and the analysis of multicomponent signals *Int. Conf. on Acoustics, Speech and Signal Process. ICASSP90* pp 2467–70

[7] Francos A and Porat M 1999 Analysis and synthesis of multicomponent signals using positive time–frequency distributions *IEEE Trans. Signal Process.* **47** 493–504

[8] Flandrin P 1999 Localisation dans le Plan Temps–Fréquence *Traitement Signal* **15** 483–92

[9] Boashash B 1992 Estimating and interpreting the instantaneous frequency of a signal (parts 1 and 2) *Proc. IEEE* **80** 520–38 and 540

[10] Rong H, Zhang G and Jin W 2007 Application of S_method to multi-component emitter signals *Proc. 33th. Ann. Conf. on IEEE Ind. Electronics Soc.* pp 2521–5

[11] Wang Y and Jiang Y 2008 Generalized time–frequency distributions for multicomponent polynomial phase signals *Signal Process.* **88** 984–1001

[12] Man'ko M A, Man'ko V I and Vilela Mendes R 2001 Tomograms and other transforms: a unified view *J. Phys. A: Math. Gen.* **34** 8321–32

[13] Man'ko V I and Vilela Mendes R 1999 Noncommutative time–frequency tomography *Phys. Lett.* A **263** 53–9

[14] Gel'fand I M, Graev M I and Vilenkin N Y 1966 5 *Generalized Functions, Integral Geometry and Representation Theory* (New York: Academic)

[15] Wood J and Barry D T 1994 Linear signal synthesis using the Radon–Wigner transform *IEEE Trans. Signal Process.* **42** 2105–11

[16] Wood J and Barry D T 1994 Radon transformation of time–frequency distributions for analysis of multicomponent signals *IEEE Trans. Signal Process.* **42** 3166–77

[17] Barbarossa S 1995 Analysis of multicomponent LFM signals by a combined Wigner–Hough transform *IEEE Trans. Signal Process.* **43** 1511–5

[18] Hugenholtz C A and Heijnen S H 1991 Pulse radar technique for reflectometry on thermonuclear plasmas *Rev. Sci. Instrum.* **62** 1100–1

[19] Laviron C, Donné A J H, Manso M E and Sanchez J 1996 Reflectometry techniques for density profiles measurements on fusion plasmas *Plasma Phys. Control Fusion* **38** 905–36

[20] Clairet F, Bottereau C, Chareau J M, Paume M and Sabot R 2001 Edge density profile measurements by X-mode reflectometry on Tore Supra *Plasma Phys. Control Fusion* **43** 429–42

[21] Clairet F, Sabot R, Bottereau C, Chareau J M, Paume M, Heureaux S, Colin M, Hacquin S and Leclert G 2001 X-mode heterodyne reflectometer for edge density profile measurements on Tore Supra *Rev. Sci. Instrum.* **72** 340–3

[22] Clairet F, Bottereau C, Chareau J M and Sabot R 2003 Advances of the density profile reflectometry on TORE SUPRA *Rev. Sci. Instrum.* **74** 1481–4

[23] Nicola De, Fedele R, Manko M A and Manko V I 2005 Fresnel tomography: a novel approach to wave-function reconstruction based on the Fresnel representation of tomograms *Theor. Math. Phys.* **144** 1206–13